

# *High Thermal Sensitivity Performance of Ferroelectric Vanadium Oxide Hybrid Process in Thermal Imaging Monitoring*

Fang Bi\*

Weifang University, Shandong, China

\*corresponding author

**Keywords:** Thermal Imaging Monitoring, Ferroelectric Vanadium Oxide, Hybrid Process, High Thermal Sensitivity

**Abstract:** Infrared focal plane array technology is a detector manufacturing technology that integrates a two-dimensional detector array on a focal plane with a multiplexed readout circuit. This research mainly discusses the high thermal sensitivity performance of the ferroelectric vanadium oxide hybrid process in thermal imaging monitoring. The choice of vanadium oxide as the material for the microbolometer is due to its high electrical resistivity, high electrical resistivity, easy manufacturing, etc., especially compatibility with silicon technology, easy mass production and low cost. In this study, a direct current magnetron sputtering technique was used to prepare undoped and Fe-doped vanadium oxide films on a glass substrate. By controlling the process parameters of magnetron sputtering, the purpose of controlling the square resistance value and resistance temperature sensitivity of the film is achieved. The vanadium target is a disc of metallic vanadium with a purity of 99.99%, a diameter of 80 mm, and a thickness of 4 mm. The specification of the patch used for doping is an Fe sheet with 99.99% purity and a size of 2mmx2.5mmx1mm. Place Fe flakes on the vanadium target, and control the concentration of doped Fe by the number of Fe flakes placed. In order to obtain high performance, the thermal array should be packaged in a vacuum envelope with an infrared emission window. Sensitive elements should not be connected to the sensitive elements of neighboring pixels to avoid thermal diffusion and loss of image resolution. When the rapid heat treatment temperature is increased to 500°C, the binding energy of the characteristic peak of V(2p<sub>3/2</sub>) drops to 516.03eV, which is in the range of VO<sub>2</sub> binding energy (515.7-516.2eV). This research will promote the application of VO<sub>2</sub> in thermal imaging monitoring.

## 1. Introduction

The excellent performance of the vanadium oxide thin film with high temperature resistivity

(absolute value of about 3%/K), low thermal conductivity, appropriate resistance and its preparation technology compatible with silicon process, makes the device, low noise, high frame, and temperature detection. The circuit is not affected by the low damage technology of vanadium oxide heat-sensitive materials, and vanadium oxide thin film materials are widely used in the fields of infrared detectors and infrared imaging.

Since the phase transition temperature of  $\text{VO}_2$  is the closest to room temperature among vanadium oxides, it has received extensive attention from researchers.  $\text{VO}_2$  single crystals often break into powder when the phase changes occur, but if it is made into a thin film, it will. This problem can be solved well, the film can also undergo repeated reversible phase changes, and the film will not be damaged during the phase change.

Ferroelectrics are expected to be used in non-volatile memory. However, difficulties in making ferroelectric layers and integrating them into complementary metal oxide semiconductor (CMOS) devices prevent rapid scaling. Mikolajick T considers hafnium oxide to be the standard material available in CMOS processes. He first reported ferroelectric properties in Si doped hafnium in 2011, reigniting interest in using ferroelectric memory for a variety of applications. Ferroelectric hafnium with mature atomic layer deposition technology is compatible with THREE-DIMENSIONAL capacitors and can solve the scaling limitation of 1-transistor-1-capacitor (1T-1C) ferroelectric random access memory (FeRAM). For ferroelectric field effect transistors (FEFETs), the low dielectric constant and high coercive field E-C of hafnium ferroelectrics are beneficial. However, the much higher e-C of ferroelectric hafnium makes high endurance a challenge. He summarized the current state of hafnium dioxide ferroelectric and explained how the material system could be used to solve the major problems of 1T-1C FeRAM and FEFET [1]. Singh D P dispersed a small amount of graphene oxide (GO) in ferroelectric liquid crystal (FLC) and has studied the effect of GO in ferroelectric liquid crystal (FLC) on the electro-optical parameters of FLC-GO composites using various techniques. Examples include Raman spectroscopy, UV-visible absorbance, XRD and polarizing microscopy. The electro-optical parameters were significantly modified, and he found that the effect was strongly dependent on cell thickness. The interlaminar electron-phonon coupling and relative orientation between GO and FLC guides are responsible for these effects. The existence of GO mainly induced the local orientation of FLC molecules at the interface, which was confirmed by X-ray diffraction results. The variation of uv absorptivity of composites is mainly due to the scattering of incident photon radiation through GO, near-crystal layer and multi-domain. His research has shown that in cases where nanomaterials are dispersed in mesocrystalline systems, cell thickness is optimized to improve the suitability of their devices, such as uv filters, and material parameters are customized by changing cell thickness [2]. Takahashi R investigated the use of thermally stabilized  $\text{Sr}_2\text{RuO}_4$  electrodes in high-temperature synthesis of oxide heterostructures. He grew atomically smooth  $\text{Sr}_2\text{RuO}_4$  films on  $\text{SrTiO}_3$  (001) substrates by pulsed laser deposition and used them as the bottom electrodes of ferroelectric  $\text{BaTiO}_3$  capacitors at temperatures up to  $1000^\circ\text{C}$ . The thermal stability of  $\text{Sr}_2\text{RuO}_4$  electrodes was verified by structural and electrical measurements of ferroelectric  $\text{BaTiO}_3$  films. It is found that the optimum growth temperature of  $\text{BaTiO}_3$  films is  $900^\circ\text{C}$ , which shows the maximum spontaneous polarization, dielectric constant and thermoelectric response.  $\text{Sr}_2\text{RuO}_4$  membranes are suitable for use as heat stable electrodes in heterostructures synthesized at temperatures up to at least  $1000^\circ\text{C}$  and oxygen pressures of  $10^{-6}$  to  $10^{-1}$  Torr. This range of growth film conditions is much wider than other common oxide electrode materials, such as  $\text{SrRuO}_3$ , and his research has thus widened the window of available processes for optimizing the performance of oxide electronics [3]. Song C believes that the emerging surface/edge electron phases driven by the effect of breaking symmetry have aroused great concern in low-dimensional

electronic systems. However, experimental evidence for their presence at the atomic scale in ferroelectric oxides is still missing. In this work, he observed the state of the metal surface on layered  $\text{Bi}_2\text{WO}_6$  by scanning tunneling microscopy/spectroscopy. The differential conductance near the edge of the step is significantly enhanced compared with that of the platform, forming a one-dimensional edge state. DFT calculations confirm that the surface symmetry break determines the electron structure, and the  $\text{O}_2\text{P}$  orbital contributes most to the density of states around the Fermi level. His findings provide a new strategy for hidden phases on the surfaces of other related oxides [4]. Yang Y believes that hole transport material (HTM) free carbon-based perovskite solar cells (C-PSC) are highly anticipated due to their simple manufacturing, but currently their power conversion efficiency (PCE) is low, mainly due to voltage loss. He reports on a new strategy to increase PCE by adding an ultra-thin layer of ferroelectric oxide  $\text{PbTiO}_3$  between the electron transport material and halide perovskite. The resulting C-PSC achieved a PCE of up to 16.37%, a record to date without HTM C-PSC, mainly due to the ferroelectric layer enhanced open-circuit voltage. Detailed measurement and analysis showed that due to the incorporation of ferroelectric  $\text{PbTiO}_3$  layer, the built-in potential in C-PSC was enhanced and non-radiative recombination was inhibited, thus improving  $v\text{-OC}$  and photovoltaic performance [5]. Liu W believes that the explosive development of the Internet of Things and wearable electronics has greatly promoted the development of diversified sensors, among which non-contact proximity sensing is of great significance for sensing various information from the environment and human body without physical contact. In theory, any remote interaction could be developed to implement proximity sensing. In recent years, proximity sensors based on field-effect transistors have been implemented, in which charged objects can be treated as grids to modulate the drain current of the transistor. However, the low carrier mobility and threshold voltage offset of organic transistors limit their sensing performance. Here, he reports an oxide semiconductor transistor approach sensor with enhanced polarization of iron electrode. The polarization state in ferroelectric layer can be adjusted well by polarization pulse of different width. Therefore, the optimal operating point of the transistor sensor is precisely controlled by the threshold voltage shift caused by iron electrode polarization. This ferroelectric-modulated oxide semiconductor transistor shows significant sensing performance against several common methods [6]. Ferroelectrics are a hot topic of research nowadays, but their research lacks data, which makes the research not rigorous enough and lacks necessary data.

This research refers to the existing preparation technology of vanadium oxide photonic crystals, combined with commonly used synthetic instruments and methods in the laboratory, to prepare ordinary vanadium oxide thin films (vanadium pentoxide thin films, vanadium dioxide thin films) and vanadium oxide thin films with ordered microstructures (Vanadium pentoxide film, vanadium dioxide film). The process parameters and annealing treatment conditions optimization during the preparation process are studied specifically, and some properties of the thin film materials are tested, characterized and theoretically analyzed. The vanadium pentoxide film was fabricated on a clean glass substrate by vertical pulling method and spin coating method, and heat treatment under different atmospheres and temperatures was carried out. The composition of the annealed film was determined by XRD, XPS and other phase characterization methods.

## 2. Thermal Imaging Monitoring Method

### 2.1. Preparation of Vanadium Dioxide

#### (1) Preparation of $\text{V}_2\text{O}_5$ Sol

First, weigh a certain amount of  $V_2O_5$  powder and dopant according to the ratio of the amount of doping element to vanadium element, grind and mix them uniformly, and place them in a porcelain crucible. Then heat at  $810^\circ\text{C}$  in a temperature muffle furnace for 20-30 minutes to melt the mixture in the crucible. By quickly pouring the molten  $V_2O_5$  in the crucible into deionized water under rapid stirring, a reddish brown  $V_2O_5$  sol is formed after water quenching, and a dark brown  $V_2O_5$  gel is formed after standing for a period of time [7].

#### (2) Preparation of doped $VO_2$ powder

$V_2O_5$ xerogel is obtained by drying the  $V_2O_5$  gel in a blast drying oven for 24h. The xerogel is heat-treated in a temperature-controlled muffle furnace at  $500^\circ\text{C}$  for 2h to obtain crystalline  $V_2O_5$ . After grinding, a yellow doped  $V_2O_5$  powder is obtained. Put the doped  $V_2O_5$  powder into a porcelain boat and place it in a tubular resistance furnace. After a constant temperature of  $500^\circ\text{C}$ , a mixed gas of  $N_2$  and  $NH_3$  is introduced, and the flow rate of  $N_2$  is controlled to  $210\text{mL}/\text{min}$ , and the flow rate of  $NH_3$  is  $15\text{mL}/\text{min}$ . Reduce under the above conditions for 1h, and then anneal the powder at  $700^\circ\text{C}$  for 5h under  $N_2$  atmosphere. Finally, it was taken out after the  $N_2$  protection dropped to room temperature, and the doped  $VO_2$  obtained was a blue-black powder [8-9].

The calculation formula of stress  $S$  is:

$$S = (\Delta\alpha)\Delta TE \quad (1)$$

$\Delta\alpha$  is the difference between the linear thermal expansion coefficient of the substrate and the film [10].

## 2.2. Thermal Imaging Monitoring

All thermal infrared detectors show changes with the temperature of the pixels. The pixels as the sensor absorb infrared radiation, and the changes in some measurable characteristics are obvious. Therefore, the analysis of various infrared detectors must start with the heat flow equation representing the temperature rise caused by the radiation power. The performance of the temperature rise depends on the detection mechanism. The most common type of probe is a pyroelectric detector resistance pyranometer that works without bias. It is called a strong dielectric coulometer or electric field enhanced pyroelectric detector and thermal neel detector. Also known as thermal radiation electronic was coupling.

Consider a focal plane array composed of two-dimensional thermal pixel components. Each pixel is composed of a sensitive area connected to the substrate, which corresponds to the infrared rays of the pixel being absorbed by the sensitive area, and the temperature rises. Heat flows from the sensitive area to its surroundings. Heat conduction has three mechanisms: conduction, convection and radiation. Conduction occurs in 3 methods within the array. Heat will flow into the substrate from the sensitive area along the support. When the sensitive areas are adjacent, heat may directly enter the adjacent pixels from the sensitive area of a specific pixel. This is called lateral heat flow. This process direction will reduce the image resolution, so it needs to be avoided.

The splash coating is based on the splash effect when charged ions hit the target, and the entire splash process is based on glow discharge. In other words, sputtering ions are generated by gas discharge. Different sputtering technologies use different glow discharge modes. Diode tripolar sputtering uses DC glow discharge. Tripolar sputtering is a glow discharge supported by a hot cathode. RF sputtering uses RF glow discharge. Magnetron sputtering is a glow discharge controlled by a circular magnetic field [11].

The change of Gibbs free energy caused by the same phase transition can be defined as [12-13]:

$$\Delta G = \Delta T_r \Delta S_0 \quad (2)$$

Among them,  $\Delta T_r$  is the offset of the phase transition temperature, and  $\Delta S_0$  is the change of entropy between the two phases before and after the phase transition [14].

The strength of the AC signal output by the test circuit is not only determined by the performance of the pyroelectric array thermal unit, but also amplified by the impedance conversion MOS tube. Since the area of the area array unit is usually tens of micrometers by tens of micrometers, and the thermal signal is small, it is usually necessary to perform a high signal-to-noise ratio pre-amplification on the output signal in practical applications. The critical size  $R$  of a steady-state nucleus can be defined as [15]:

$$R = 2\gamma(\Delta T_r \Delta S_0) \quad (3)$$

The development of infrared imaging array and signal readout and detection are important contents of uncooled infrared imaging technology. According to the characteristics of high impedance of inorganic nano-ceramics and polyvinylidene fluoride-trifluoroethylene composite sensitive film capacitive elements, the MOS field effect tube is designed as the sensitive element for impedance conversion, and the unidirectional conduction characteristic of the same integrated diode is used to meet the sensitivity of the imaging array. The on-chip polarization requirements of the components can improve the readout sensitivity. The series MOS tube is used for the on-off isolation of each element, and the dual 16-stage shift register is used for the addressing control of the integrated pyroelectric array in the X and Y directions to ensure the reliable readout of the 16X16 area array infrared imaging signal. Phase speed ratio [16]:

$$V = \lambda v \exp -\Phi / kT \quad (4)$$

Among them, is the activation energy of the  $\Phi$  barrier, defined as:

$$\Phi = kT_R \quad (5)$$

Where  $k$  is Boltzmann's constant and  $T_R$  is the phase transition temperature [17].

Adding certain metal or non-metal elements to the  $\text{VO}_2$  film can change the phase transition temperature of the  $\text{VO}_2$  film. The influence factors of different doping ions on the phase transition temperature are shown in Table 1. In addition, the phase variable of the phase transition temperature is proportional to the amount of doping elements added.

*Table 1. Influence factors of different doping ions on phase transition temperature*

Doped elements (atomic ratio at%)	$\text{W}^{6+}$	$\text{Mo}^{6+}$	$\text{Ta}^{5+}$	$\text{Nb}^{5+}$
Phase transition temperature change ( $^{\circ}\text{C}$ )	-23	-15	-5~- 10	-7.8
Doped elements (atomic ratio at%)	$\text{AF}^{3+}$	$\text{Ga}^{3+}$	$\text{Fe}^{3+}$	$\text{Cr}^{3+}$
Phase transition temperature change ( $^{\circ}\text{C}$ )	+9	+6.5	+3	+3

### 2.3. Preparation of Fe-Doped Vanadium Oxide Film

This experiment uses DC magnetron sputtering technology to prepare undoped and Fe-doped vanadium oxide thin films on a glass substrate. The vanadium target is a disc of metallic vanadium with a purity of 99.99%, a diameter of 80 mm, and a thickness of 4 mm.

Compared with other coating methods, sputtering coating method has the following advantages:

(1) The thickness of the film is better controlled, and a film with better uniformity can be obtained on a larger area. The particles of the film are relatively uniform and the distribution is relatively dense, which is easy to obtain a high-quality film;

(2) The film has good repeatability. Since the film deposition process is all automated processes, as long as the process parameters are strictly controlled, a reproducible film can be obtained;

(3) Strong adhesion between the film and the substrate. During the sputtering process, the energy of the atom is very high. When it is deposited on the substrate, the energy it carries generates a large amount of heat energy to increase the temperature of the substrate, and a higher substrate temperature will increase the adhesion of the film to the substrate. At the same time, part of the sputtered atoms hit the surface of the substrate to cause injection, thereby forming a pseudo-diffusion layer on the substrate where the sputtered atoms and the substrate atoms are fused with each other. In addition, during the film deposition process, the substrate is always cleaned and activated in the plasma area, which not only removes the sputtered atoms with weak adhesion, but also allows the surface of the substrate to be continuously purified, thereby enhancing the adhesion of the film.

(4) High film purity. Since other impurities are not introduced in the sputtering method, the purity of the film obtained by sputtering is very high. But the sputtering method also has its own shortcomings, such as low deposition rate, high substrate temperature, strict working gas requirements, complex equipment structure, and large equipment investment. However, due to the improvement of the technological level in recent years and the continuous increase of research efforts, the radio frequency sputtering and magnetron sputtering technology has been greatly developed, which has made improvements in increasing the sputtering speed and reducing the substrate temperature. The sputtering coating equipment is shown in Figure 1.

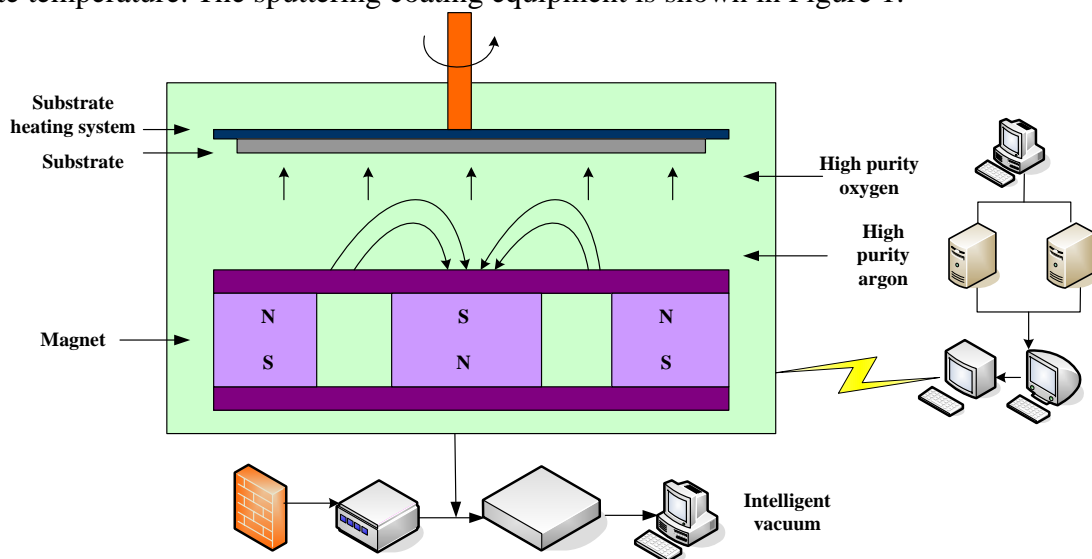


Figure 1. Sputtering coating equipment

Patch method: Using the principle of the damascene method, the doping material is directly placed on the metal target for sputtering, and the doping concentration is controlled by controlling the coverage area of the doping material on the metal target. The operation is simple and the metal is avoided. Therefore, in this study, the patch method was used to prepare doped vanadium oxide films. The names, specifications and purity of the main raw materials and drugs used in the experiment are shown in Table 2.

*Table 2. The name, specification and purity of the main raw materials and drugs used in the experiment*

Raw material/reagent name	Chemical formula	Molecular weight	Specification and purity
Vanadium pentoxide	V <sub>2</sub> O <sub>5</sub>	181.88	500g/4N
Oxalic acid	C <sub>2</sub> H <sub>2</sub> O <sub>4</sub> ·2H <sub>2</sub> O	126.07	500g/AR
Hydrochloric acid	HCl	36.46	500ml/AR
Hydrazine Hydrochloride	N <sub>2</sub> H <sub>4</sub> ·2HCl	104.9	100g/AR
Ammonium Carbonate	NH <sub>4</sub> HCO <sub>2</sub>	79.06	500g/AR
Sodium Tungstate	Na <sub>2</sub> WO <sub>4</sub> ·2H <sub>2</sub> O	329.86	500g/AR
Nitric acid	HNO <sub>3</sub>	63.01	500ml/AR
Hydrazine hydrate (85%)	N <sub>2</sub> H <sub>4</sub> H <sub>2</sub> O	50.06	500m/AR
Absolute ethanol	C <sub>2</sub> H <sub>5</sub> OH	46.07	500m/AR
Anhydrous ether	C <sub>4</sub> H <sub>10</sub> O	74.15	500ml/AR
Carbon dioxide	CO <sub>2</sub>	44	99.99%
High purity nitrogen	N <sub>2</sub>	34	99.99%

The specification of the patch used for doping is an Fe sheet with 99.99% purity and a size of 2mm×2.5mm×1mm. Place Fe flakes on the vanadium target, and control the concentration of doped Fe by the number of Fe flakes placed. Before the sputtering experiment, the cleaned glass slides were taken out from the absolute ethanol solution, dried with high-pressure nitrogen (N<sub>2</sub>) and placed in the reaction chamber quickly. During the sputtering process, high-purity working gas argon (Ar) and reaction gas oxygen (O<sub>2</sub>) are introduced into the chamber through their respective mass flow meters. After the pressure in the reaction chamber reached 18×10<sup>3</sup>Pa, the sputtering experiment was started. The current used for sputtering was 0.34A, and the substrate temperature was kept at 60°C during the sputtering process. The vanadium target will be pre-sputtered for 15 minutes in an argon (Ar) atmosphere to remove residual oxides on the surface of the vanadium target. During the formal sputtering, the Ar/O<sub>2</sub> flow ratio is 98:1, and the sputtering current remains unchanged. Other experimental conditions for preparing vanadium oxide thin films and the Fe doping concentration measured by XPS (X-ray photoelectron spectrometer) are shown in Table 3.

Table 3. Other experimental conditions for preparing vanadium oxide thin films and the Fe doping concentration measured by XPS (X-ray photoelectron spectrometer)

Sample	Sputtering time (min)	Annealing temperature (°C)	Annealing time (min)	Annealing oxygen flow (SCCM)	Number of Fe slices	Fe doping concentration (at%)
S1	15	450	30	15	0	0
S2	15	450	30	15	1	32
S3	15	450	30	15	2	6.9
S4	15	450	30	15	3	9.8
S5	15	450	30	15	4	12.0

The integral transmittance is used to calculate the visible light transmittance of the VO<sub>2</sub> thermochromic smart window, the formula is as follows [18]:

$$T_{lum} = \int \Phi(\lambda)T(\lambda)d\lambda / \int \Phi_{lum}(\lambda)d\lambda \quad (6)$$

$\Phi_{lum}(\lambda)$  is the human vision function, and  $T(\lambda)$  is the transmittance value of VO<sub>2</sub> at the wavelength  $\lambda$  [19]. The integral transmittance can be used to calculate the solar transmittance  $T_G$  of VO<sub>2</sub> in the entire solar spectrum (250-2600nm):

$$T_G = \int \beta(\lambda)T(\lambda)d\lambda / \int T(\lambda)d\lambda \quad (7)$$

Among them,  $\beta(\lambda)$  is the solar radiation spectrum when the air quality is 1.5 [20].

The difference between the low temperature sunlight transmittance  $T_{SOL,G}$  and the high temperature sunlight transmittance  $T_{SOL,D}$  [21]:

$$\Delta T_{SOL} = T_{SOL,G} - T_{SOL,D} \quad (8)$$

In fact, actual infrared detectors, especially integrated sensors, cannot use a large area: not only the dielectric loss of the sensitive film, but also the heat loss caused by conduction and convection; the absorption coefficient of the absorption layer can only be less than 1 and the temperature change of the sensitive film caused by infrared radiation will have a gradient distribution: in order to detect, the sensitive element must be impedance matched and signal amplified. Therefore, the detection rate value of the ideal detector mentioned above is only the theoretical limit value.

## 2.4. Characterization Techniques Required for Experiments

### (1) X-ray powder diffraction (XRD)

This article uses the X-ray diffractometer model DMax-2200 provided by Rigaku, and is equipped with a high temperature accessory (normal temperature 1000 °C) for experimental observation. Its main technical specifications are: copper target (Cu-K $\alpha$ , 1.54056Å); tube pressure 40kV, tube flow 80mA; scanning speed 0.39°/s.

### (2) Transmission electron microscope (TEM)

This article uses the transmission electron microscope model JEM 0200CX provided by JEOL. Its main technical specifications are: dot resolution 0.19nm; magnification  $\times 50 \sim 1500000$ ; acceleration voltage 80-200kV.

## (3) X-ray photoelectron spectroscopy (XPS)

This article uses Perkin-Elmer's PHI 5000C ESCA system photoelectron spectrometer. Its main technical parameters are: The background pressure of the system is better than  $1 \times 10^{-7}$  Pa, Al and  $K\alpha$  rays ( $h\nu=1486.6\text{eV}$ ), power 250W, The working voltage is 14.0 kV, and the binding energy is based on the C1s binding energy of surface pollution carbon ( $BE=284.5\text{eV}$ ).

## (4) Energy Dispersive X Fluorescence Spectroscopy (EDX)

This paper uses the EDX attached to the JSM 6460 SEM produced by JEOL for analysis. The instrument's low vacuum mode resolution is 4.0nm, the acceleration voltage is 30KV, the magnification is  $\times 300000$ , and the sample stage is: X=125mm, Y=100mm.

## (5) Thermogravimetric-differential thermal analysis method (TG-DTA)

This paper uses the American Perkin-Elmer Pyris Diamond TG-DTA thermal analyzer, N2 atmosphere protection, nitrogen flow rate 20ml/min, heating rate  $5^\circ\text{C}/\text{min}$ .

### 3. Process Research Results

However, strictly speaking, the preparation of  $\text{VO}_2$  films by the method of low-temperature deposition followed by high-temperature annealing is not a true "low-temperature preparation" method. Although the film is deposited at a relatively low temperature, it still needs a follow-up high-temperature annealing process. In addition, this process requires one more annealing process than direct deposition, which increases the possibility of film contamination. The parameters of the high-temperature annealing process are shown in Figure 2.

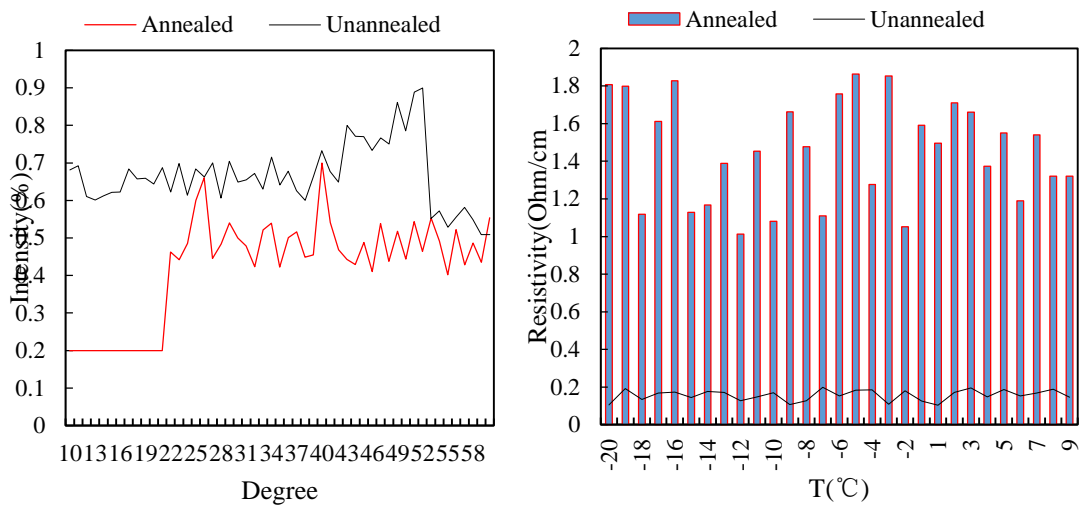


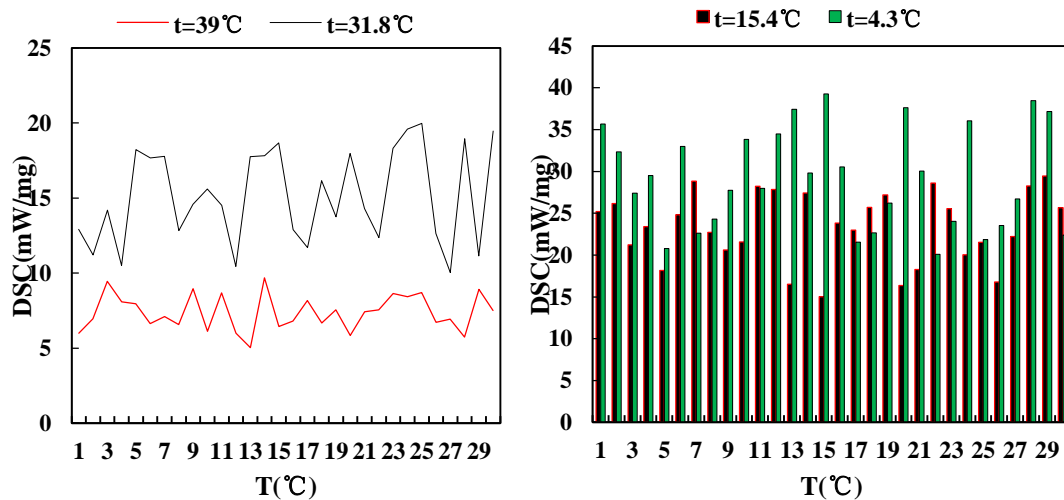
Figure 2. High temperature annealing process parameters

It is worth noting that the optical properties of the single-layer  $\text{VO}_2$  film obtained at a high temperature of  $450^\circ\text{C}$  are  $T=36.4\%$  and  $\Delta T_{\text{soL}}=7.8\%$ . Therefore, the  $40\text{nmCr}_2\text{O}_3/\text{VO}_2$  film prepared at a low temperature of  $275^\circ\text{C}$  has an improved visible light transmittance and solar light regulation efficiency compared with a single-layer  $\text{VO}_2$  film prepared at a high temperature of  $450^\circ\text{C}$ . The changes of different parameters are shown in Table 4.

Table 4. Variations of different parameters

Sample	$\beta(\lambda)$	$T(\lambda)$	$T_{SOL,D}$	$T_{SOL,G}$	$\Delta T_{SOL}$
VO <sub>2</sub> -4509°C	36.4	37.3	42.1	34.3	7.8
VO <sub>2</sub> -275°C	42.4	42.6	36.3	35.9	0.4
20nm Cr <sub>2</sub> O <sub>3</sub> /VO <sub>2</sub> -275°C	39.5	38.8	36.2	32.9	5.1
40nm Cr <sub>2</sub> O <sub>3</sub> /VO <sub>2</sub> -2759°C	43.9	42.3	39.1	33.8	6.2
60nm Cr <sub>2</sub> O <sub>3</sub> /VO <sub>2</sub> -275°C	47.8	43.2	42.1	34.8	8.3

Figure 3 shows the DSC of VO<sub>2</sub> with different Na<sub>2</sub>WO<sub>4</sub> doping levels. It can be clearly seen from that the phase transition temperatures corresponding to Na<sub>2</sub>WO<sub>4</sub> doping from 0.5% to 2.0% are 49.0°C, 31.8°C, and 15.4°C, respectively. And 4.3°C, the corresponding enthalpy values are 15.2J/g, 13.2J/g, 9.1J/g and 4.4J/g, respectively. It shows that Na<sub>2</sub>WO<sub>4</sub> as a dopant has a very obvious effect on reducing the phase transition temperature. Fitting the above iron doping amount to the phase transition temperature data, it is found that as the iron doping amount increases, the phase transition temperature decreases linearly, and the average doping 1at.%Na<sub>2</sub>WO<sub>4</sub>, phase transition temperature of VO<sub>2</sub> is reduced by about 32°C. This is much better than using W as the dopant to decrease the phase transition temperature by 26K/at.%.

Figure 3. DSC of VO<sub>2</sub> with different Na<sub>2</sub>WO<sub>4</sub> doping levels

It can be seen from Figure 4 that the diffraction peaks of all doped samples and the low-temperature monoclinic phase VO<sub>2</sub>(M) (space group: P21/c, a=5.752Å, b=4.538Å, c=5.383Å, JCPDS Card: 43-1051) is basically corresponding, indicating that the prepared powders are all homogeneous VO<sub>2</sub>(M) powders, and there is no vanadium oxide phase of other valence states. The diffraction peaks and low-temperature monoclinic of the sample are shown in Figure 4.

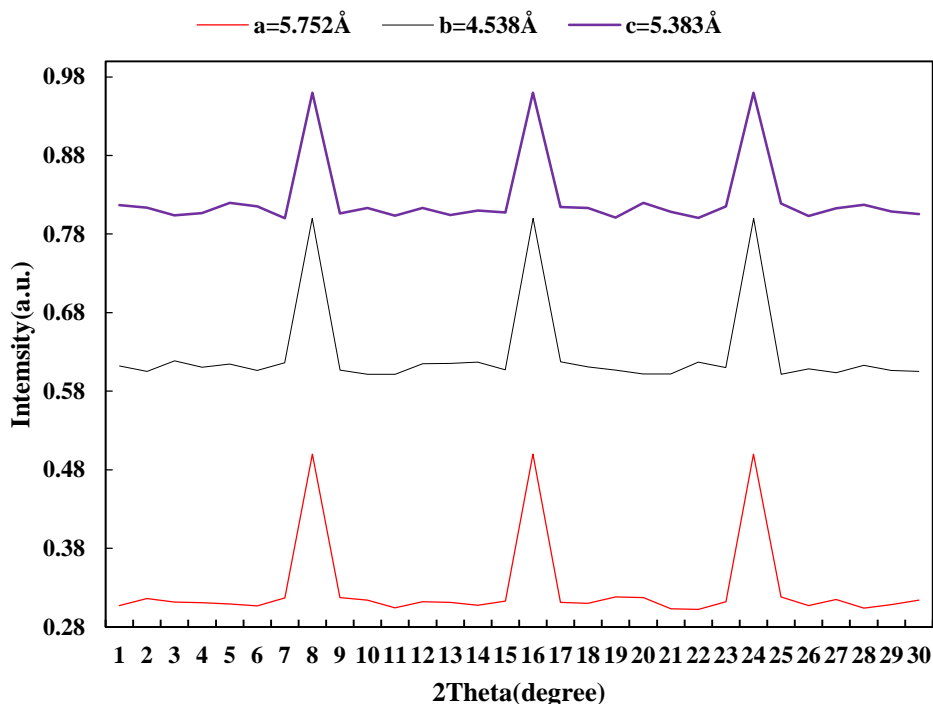


Figure 4. Diffraction peak and low-temperature monoclinic of the sample

The TG-DTA thermal analysis method is used to make its thermal weight loss (TG) and differential thermal analysis (DTA) curves to determine the thermal decomposition conditions of the powder. The thermogravimetric and differential thermal (TG-DTA) curve of the precursor in a  $N_2$  atmosphere at a heating rate of  $5^\circ\text{C}/\text{min}$  is shown in Figure 5.

During the thermal decomposition process at  $50\text{--}350^\circ\text{C}$ , 4 intermediates S1, S2, S3 and S4 appeared, until the target product  $\text{VO}_2$  was formed at  $346.5^\circ\text{C}$ . Different thermal decomposition reactions took place in 4 stages. Each decomposition process corresponding to the TG curve will lose a certain amount of quality. When the temperature is  $85.9^\circ\text{C}$ , the TG curve loses 12.3% of the weight. This process involves the evaporation of water and the release of carbon dioxide: When the temperature is  $164.1^\circ\text{C}$ , the TG curve loses 20.2% of the weight, indicating that the mass loss in this process may be caused by decomposition of excess oxalic acid in the precursor and the loss of crystal water of vanadyl (IV) basic ammonium carbonate: When the temperature is  $273.2^\circ\text{C}$ , the weight loss of TG curve is 10.0%, indicating that this process is vanadyl (IV) basic carbonic acid The process of thermal decomposition of ammonium. The broad peak corresponding to  $301.1^\circ\text{C}$  corresponds to the final product  $\text{VO}_2$ . The exothermic peak at  $346.5^\circ\text{C}$  is attributed to the exothermic effect of  $\text{VO}_2$  crystallization.

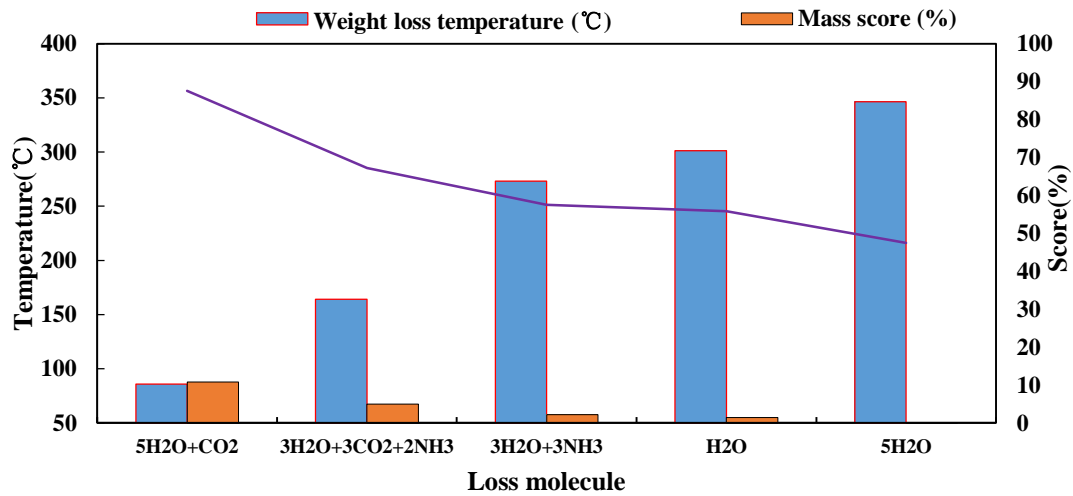


Figure 5. Thermogravimetric and differential heating (TG-DTA) curve under the condition of 5 °C/min heating rate

The samples before and after the rapid heat treatment were also analyzed by XPS high-resolution spectroscopy. As shown in Figure 6, the binding energy of the characteristic peak of V(2p<sub>3/2</sub>) decreased from 517.15eV before heat treatment to 516.57eV after rapid heat treatment at 350°C/30s. The VO<sub>x</sub> film under these two conditions is still dominated by the high valence state V content. When the rapid heat treatment temperature is increased to 500°C, the binding energy of the characteristic peak of V(2p<sub>3/2</sub>) drops to 516.03eV, which is at the VO<sub>2</sub> binding energy. In the interval (515.7-516.2eV), the film is dominated by V<sub>4+</sub>.

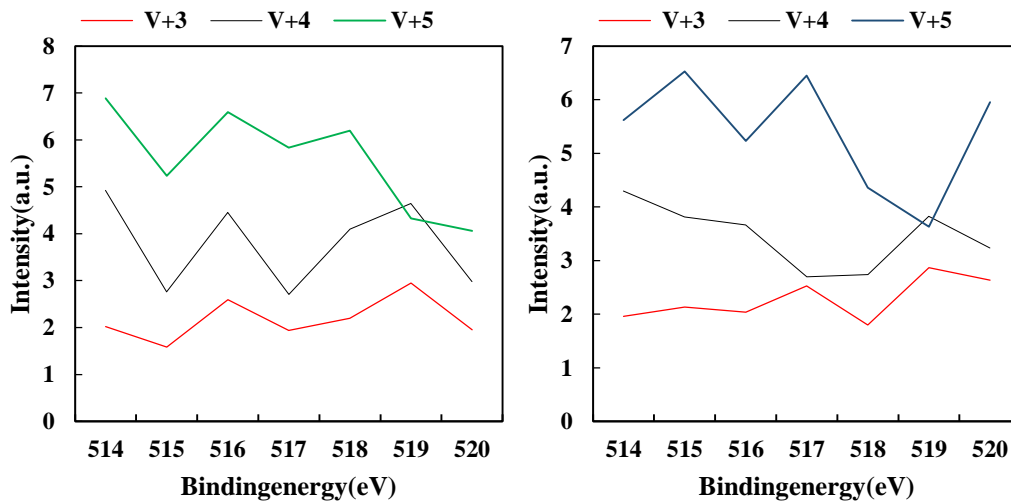


Figure 6. The same XPS high-resolution atlas analysis of samples before and after rapid heat treatment

#### 4. Discussion

In the structure of vanadium dioxide, there is an oxygen atom that is closer to the vanadium atom, and the other oxygen atoms are farther away from the vanadium atom, so there is a bond similar to

V=O. When the VO<sub>2</sub> film undergoes a phase transition from low temperature to high temperature, it changes from a monoclinic symmetrical distortion rutile structure to a tetragonal rutile structure. The phase transition temperature is inconsistent [22-23].

After the VO<sub>2</sub> film is heated, the resistance of the film gradually decreases as the temperature increases, but the rate of decrease is very slow. If the temperature continues to rise to the phase transition temperature region, the resistance of the film decreases sharply as the temperature rises. In addition, if the temperature rises to a certain extent, the resistance of the film decreases as the temperature rises. At this time, if the film cools, the resistance of the film increases. When the temperature drops to near the phase transition temperature, the resistance of the film increases rapidly with the decrease in temperature. If the temperature drops, the rate of increase in resistance will start to slow down. If the temperature drops, the resistance value may return to the original low temperature value. The manufacturing process of the vanadium oxide film has a great influence on the performance of the film. By choosing an appropriate preparation process, not only can the performance of the film be improved, but also the cost and efficiency can be reduced. Among them, reactive sputtering and heat treatment are one of the most widely used methods for preparing vanadium oxide thin films. The film produced by this method has high purity, good compactness, and good bonding with the substrate, but there are many limiting parameters, such as the ratio of argon and oxygen directly affecting the characteristics of the film, and the production process is relatively complicated. The article studies new methods. First, the vanadium metal thin film is directly produced by sputtering. Then, a rapid thermal oxidation treatment was performed in a pure oxygen environment through a rapid thermal treatment device. After that, in order to improve the phase transformation characteristics, a rapid annealing treatment in a pure nitrogen environment was used. There is only one gas used in each heat treatment process, and the preparation process is relatively simple. On this basis, the effects of heat treatment conditions and substrates on the phase transition characteristics of vanadium oxide thin films include 4 detection and test techniques, THz time-domain spectroscopy system, atomic force microscope, X-ray diffractometer, and X-ray photoelectron spectroscopy [24].

Among a variety of vanadium oxides, at least 8 have thermally induced phase transition properties, but due to the different atomic arrangement and lattice structure of each oxide, they have unique phase transition properties and also have optical and electrical properties caused by phase transition properties. The development of mechanical optical switches is very mature. The traditional mechanical optical switches have low insertion loss and high insulation, but the switching time is long. The further development of a large number of new types of mechanical types that are not compatible with microelectronics technology is greatly restricted. Optical switches based on microelectronics technology not only combine the advantages of traditional mechanical optical switches, but also have the advantages of small capacity. Non-mechanical optical switches use thermo-optic, electro-optic, and acousto-optic effects to change the waveguide refractive index of the switching medium. Due to the excitation of heat and light, the internal structure of vanadium oxide changes, and the light transmittance also changes significantly. This is a non-mechanical optical switch material with huge possibilities hidden [25-26].

The vanadium metal film is produced by magnetron spraying method, using high-purity argon gas, and the experimental control of other process conditions remains unchanged. Only by changing the spraying time, the thickness of the vanadium metal film can be changed to produce metal vanadium. Because the film is easy to oxidize, the splash deposition time is not long, so the splash time is selected as 10 minutes of the metal film for further research. The effect of heat treatment process conditions on film properties. The highly oriented V<sub>2</sub>O<sub>5</sub> film can be made on the Si/SiO<sub>2</sub>

substrate by the sol-gel method, but the substrate must have good hydrophilicity. Unlike other methods such as thermal evaporation, if the concentration of the sol is not high and the film is not too thick at one time, the film can be crystallized at various temperatures and various atmospheres [27].

Traditional ion beam enhanced evaporation (IBED) is the physical process of the interaction between the main implanted ions and the target atoms. This physical process is mainly reflected in the doping effect and damage effect of the implanted ions on the impacted target, and the mixing of the interface between the deposited film and the substrate due to the influence of the implanted target atom's ions. The argon injection beam mainly reflects physical effects. In other words, due to the damage effect of argon injection, the V-O bond of the  $V_2O_5$  film deposited by sputtering is destroyed, so O can be reduced by hydrogen injection at a lower temperature. Since argon does not combine with other atoms, the doping effect of argon will only introduce stress in the deposited film. As a result, the heat resistance curve of the  $VO_2$  film becomes larger, and the temperature coefficient of the thermal resistance of the film at room temperature will also increase. At the same time, the high-dose argon impact also densifies the film deposited by sputtering, greatly improving the adhesion between the film and the substrate. The purpose of hydrogen ion implantation is mainly to reflect chemical effects. The injected hydrogen combines with the oxygen precipitated by the argon impact damage, reducing the order of the deposited  $V_2O_5$  film, and finally generates a  $VO_2$  film. In order to reduce the sputtering deposition of  $V_2O_5$  film, the correlation between physical interaction and chemical interaction must be strictly controlled to adjust the relationship with the impact of the argon-hydrogen mixed ion beam. In other words, the sputtering deposition rate and injection conditions must be strictly controlled [28].

In the case of ion beam enhanced accumulation, the injected argon ions cannot become replacement atoms and have no valence, but can only exist in the form of intermittent atoms in the crystal or in the form of free radicals (bubbles) in the particle boundary. Therefore, the description of the size of the atom and the high or low valence of the atom does not apply. However, due to the presence of argon, stress will be generated at the intermittent position and the position of the grain boundary, and the atomic arrangement of the  $VO_2$  structure will be deformed. Therefore, the energy band overlap of the D electron in the outer layer of the V atom may occur at a low temperature. This needs to change from semiconductor to metallic phase. The output signal of the infrared imaging array uses an absolute black body as an infrared source, converts it into an AC signal incident on the array, uses a switch to detect the output signal, and uses a phase lock-in amplifier to measure the output signal. As a heat source, infrared rays can also be obtained by heating the silicate rod as a filter. Because this array is three-dimensional integration, the incidence of a laser source will induce photoelectric effect and change the working state of the MOS device in the readout circuit, so laser measurement cannot be used.

## 5. Conclusion

$VO_2$  can undergo phase transition characteristics of semiconductors and metals, and cause sudden changes in properties such as optics, electricity, and magnetism. Its phase transition temperature is very close to room temperature, so it has a wide range of applications. How to prepare a  $VO_x$  film with obvious phase change characteristics and study its phase change characteristics has become an academic hotspot in recent years. In this study,  $VO_x$  films were prepared by magnetron sputtering on  $SiO_2/Si$  and Fe substrates. By changing the sputtering time, Ar/ $O_2$  ratio, and changing the rapid heat treatment process, the  $VO_x$  film with excellent phase

change characteristics was studied. The preparation process of VO<sub>x</sub> was film. In the study, SEM, AFM, XRD, XPS and other modern microscopic analysis methods were used to analyze the surface morphology, microstructure, crystalline state of vanadium oxide in the film and the valence state of V in the VO<sub>x</sub> film. (011) VO<sub>2</sub> with crystal orientation is the main component in the film, which is the main reason for the phase change of the film. Under the currently known process conditions, further study the effect of the heating rate, working gas flow rate and other process conditions in the heat treatment process on the properties of the vanadium oxide film. Reduce the thin film preparation process, and study how to prepare vanadium oxide thin films with high phase change characteristics through rapid heat treatment in a pure oxygen environment.

### Funding

This article is not supported by any foundation.

### Data Availability

Data sharing is not applicable to this article as no new data were created or analysed in this study.

### Conflict of Interest

The author states that this article has no conflict of interest.

### References

- [1] Mikolajick T, Slesazek S, Park M H, et al. Ferroelectric hafnium oxide for ferroelectric random-access memories and ferroelectric field-effect transistors. *MRS Bulletin*, 2018, 43(05):340-346. <https://doi.org/10.1557/mrs.2018.92>
- [2] Singh D P, Kumar V, Kumar A, et al. Effect of graphene oxide interlayer electron-phonon coupling on the electro-optical parameters of a ferroelectric liquid crystal. *Rsc Advances*, 2017, 7(21):12479-12485. <https://doi.org/10.1039/C6RA25126A>
- [3] Takahashi R, Lippmaa M. Thermally Stable Sr<sub>2</sub>RuO<sub>4</sub> Electrode for Oxide Heterostructures.. *Acs Appl Mater Interfaces*, 2017, 9(25):21314-21321. <https://doi.org/10.1021/acsami.7b03577>
- [4] Song C, Gao J, Liu J, et al. Atomically Resolved Edge States on a Layered Ferroelectric Oxide. *ACS Applied Materials & Interfaces*, 2020, 12(3):4150-4154.
- [5] Yang Y, Liu Z, Ng W K, et al. An Ultrathin Ferroelectric Perovskite Oxide Layer for High-Performance Hole Transport Material Free Carbon Based Halide Perovskite Solar Cells. *Advanced Functional Materials*, 2019, 29(1):1806506.1-1806506.10.
- [6] Liu W, Lin D, Chen Q, et al. Ferroelectric Polarization Enhancement of Proximity Sensing Performance in Oxide Semiconductor Field-Effect Transistors. *ACS Applied Electronic Materials*, 2020, 2(10):3443-3453.
- [7] Chen Y H, Su C J, Hu C, et al. Effects of Annealing on Ferroelectric Hafnium Zirconium Oxide-Based Transistor Technology. *IEEE Electron Device Letters*, 2019, 40(3):467-470. <https://doi.org/10.1109/LED.2019.2895833>
- [8] Si M, Xiao L, Ye P D. Ferroelectric Polarization Switching of Hafnium Zirconium Oxide in a Ferroelectric/Dielectric Stack. *ACS Applied Electronic Materials*, 2019, 1(5):745-751.
- [9] Matveyev Y, V Mikheev, Negro V D, et al. Polarization-dependent electric potential

- distribution across nanoscale ferroelectric  $\text{Hf}_{0.5}\text{Zr}_{0.5}\text{O}_2$  in functional memory capacitors. *Nanoscale*, 2019, 11(42):19814-19822. <https://doi.org/10.1039/C9NR05904K>
- [10] Wang X W , Sun L Y , Wang X E , et al. A facile hot plate annealing at low temperature of  $\text{Pb}(\text{Zr}_{0.52}\text{Ti}_{0.48})\text{O}_3$  thin films by sol-gel method and their ferroelectric properties. *Journal of Materials Science: Materials in Electronics*, 2018, 29(7):5660-5667. <https://doi.org/10.1021/acsaelm.0c00702>
- [11] Liao W , Huang X , Coillie F V , et al. Processing of Multiresolution Thermal Hyperspectral and Digital Color Data: Outcome of the 2014 IEEE GRSS Data Fusion Contest. *IEEE Journal of Selected Topics in Applied Earth Observations & Remote Sensing*, 2017, 8(6):2984-2996.
- [12] Ikehata M , Kawashita M . An inverse problem for a three-dimensional heat equation in thermal imaging and the enclosure method. *Inverse Problems & Imaging*, 2017, 8(4):1073-1116.
- [13] Roopaei M , Rad P , Choo K . Cloud of Things in Smart Agriculture: Intelligent Irrigation Monitoring by Thermal Imaging. *IEEE Cloud Computing*, 2017, 4(1):10-15. <https://doi.org/10.1109/MCC.2017.5>
- [14] Cho Y , Julier S J , Marquardt N , et al. Robust tracking of respiratory rate in high-dynamic range scenes using mobile thermal imaging. *Biomedical Optics Express*, 2017, 8(10):4480-4503. <https://doi.org/10.1364/BOE.8.004480>
- [15] Min S , Heo J , Kong Y , et al. Thermal Infrared Image Analysis for Breast Cancer Detection. *Ksii Transactions on Internet & Information Systems*, 2017, 11(2):1134-1147.
- [16] Alkali A H , Saatchi R , Elphick H , et al. Thermal image processing for real-time non-contact respiration rate monitoring. *Iet Circuits Devices & Systems*, 2017, 11(2):142-148. <https://doi.org/10.1049/iet-cds.2016.0143>
- [17] Lee E K , Viswanathan H , D Pompili. Model-Based Thermal Anomaly Detection in Cloud Datacenters Using Thermal Imaging. *IEEE Transactions on Cloud Computing*, 2018, 6(99):330-343.
- [18] Sousa E , Vardasca R , Teixeira S , et al. A review on the application of medical infrared thermal imaging in hands. *Infrared Physics & Technology*, 2017, 85(2017):315-323.
- [19] Zhang S , Shang S , Han Y , et al. Ex Vivo and In Vivo Monitoring and Characterization of Thermal Lesions by High-Intensity Focused Ultrasound and Microwave Ablation Using Ultrasonic Nakagami Imaging. *IEEE Transactions on Medical Imaging*, 2018, 37(7):1701-1710. <https://doi.org/10.1109/TMI.2018.2829934>
- [20] Zadeh H G , Dadpay M , Namdari F , et al. Providing a model for the diagnosis of varicocele in the scrotum thermal images. *Biomedical Research*, 2017, 28(9):4049-4052.
- [21] Yang F , D Chen , Guo Z F , et al. The application of novel nano-thermal and imaging techniques for monitoring drug microstructure and distribution within PLGA microspheres. *International Journal of Pharmaceutics*, 2017, 522(1-2):34-49.
- [22] Yin X , Wang H , Jiang T , et al. Up-conversion luminescence properties and thermal effects of  $\text{LaVO}_4:\text{Er}^{3+}$  under 1550 nm excitation. *Materials Research Bulletin*, 2017, 86(FEB.):228-233.
- [23] Sniegowski M C , Erlanger M , Olson J . Thermal imaging of corneal transplant rejection. *International Ophthalmology*, 2017, 38(6):1-5.
- [24] Stephanie, Bennett, Tarek, et al. Adaptive Eulerian Video Processing of Thermal Video: An Experimental Analysis. *IEEE Transactions on Instrumentation and Measurement*, 2017, 66(10):2516-2524. <https://doi.org/10.1109/TIM.2017.2684518>

- [25] Shannon, Jidas. *Compact Thermal Imaging. Intersec: The journal of international security*, 2018, 28(9):20-22.
- [26] Eugene, Nielsen. *Thermal Imaging on Your Smartphone. S.W.A.T.: special weapons & tactics for the prepared American*, 2017, 36(5):84-88.
- [27] Larsson J , Jansson A , Karlsson P . *Monitoring and evaluation of the wire drawing process using thermal imaging. The International Journal of Advanced Manufacturing Technology*, 2019, 101(5):2121-2134. <https://doi.org/10.1007/s00170-018-3021-7>
- [28] Soong R , Jenne A , Biswas R G , et al. *Exploring the Maker Culture in Chemistry: Making an Affordable Thermal Imaging System for Reaction Visualization. Journal of Chemical Education*, 2020, 97(10):3887-3891. <https://doi.org/10.1021/acs.jchemed.0c00516>